International Journal of Applied Mechanics
(2023) 2350010 (17 pages)

DOI: 10.1142/S1758825123500102

Numerical Investigation of Cavitation Flow Characteristics in a Hydrodynamic Levitated Micropump with Eccentric Rotation

Song Xue, Guanying Xing, Tao Hong, Huaiyu Zuo and Xiaobing Luo*

School of Energy and Power Engineering
Huazhong University of Science and Technology
Wuhan 430074, P. R. China
**luoxb@hust.edu.cn*

Received 2 August 2022
Revised 23 November 2022
Accepted 10 December 2022
Published

In this study, the anti-cavitation performance and cavitation flow characteristics in a hydrodynamic levitated micropump were investigated based on numerical simulation and experiment. The cavitation characteristic curves and the development process of cavitation in the levitated micropump was firstly analyzed. Special emphasis was put on the effects of eccentricity on the anti-cavitation performance. The results show that as the eccentricity increases, the critical cavitation number gradually decreases, indicating that the eccentric rotation is beneficial to improve the anti-cavitation ability of the levitated micropump. The coupling effects between the radial force on the impeller and cavitation were also numerically studied. With the decrease of cavitation number, the radial force on the impeller gradually declines at first, then has a sudden increase and finally reduces with fluctuation. The drop of the radial force will lead to the decrease of eccentricity, resulting in the deterioration of cavitation further. In addition, the unsteady pressure pulsation was analyzed. The predominant frequencies of pressure pulsation are the blade passing frequency (BPF) and the harmonic frequency of BPF under both noncavitation and critical cavitation. Under critical cavitation, the amplitude of BPF has a drop, while the amplitude of low frequency less than BPF becomes larger.

Keywords: Hydrodynamic levitated micropump; cavitation; eccentricity; radial force; pressure pulsation.

1. Introduction

As the power source of microfluidic systems, micropumps are widely used in chemical analysis, biological and chemical sensing, drug delivery, electronic cooling and aerospace [Mohith *et al.*, 2019; Nguyen *et al.*, 2002; Woias, 2005; Hatami *et al.*, 2020]. Among all kinds of micropumps [Laser and Santiago, 2004], the mechanically centrifugal pump is a promising choice for microfluidic systems because of

*Corresponding author.

its mature manufacturing techniques. When the centrifugal pump is miniaturized, rotating speed needs to be increased to obtain higher power density. However, the traditional centrifugal micropump suffers from the contact bearing wear failure due to mechanical friction between the moving parts. And higher rotating speed even deteriorates the bearing wear, causing great declines in reliability and lifetime. To avoid the problem completely, we proposed a hydrodynamic levitated centrifugal micropump in our previous works [Luo *et al.*, 2016b, 2017a,b,c]. Relying on the suspension forces provided by the radial journal bearing and the axial thrust bearings, the rotor can be stably suspended in the surrounding fluid without any contact with other components, thus, acquiring long life and high reliability.

However, the levitated micropump was found to be faced with cavitation problems in practical applications, which is inevitable in centrifugal pumps [Cao *et al.*, 2022; Luo *et al.*, 2016a]. Cavitation refers to the formation of vapor cavities when the local static pressure falls below the vaporization pressure of the liquid and the collapse of vapor cavities during the flow. Consequently, the occurrence of cavitation is strongly correlated to the local pressure drop and the rising vaporization pressure. Lu *et al.* [2016] found that vapor bubbles initially occurred near the leading edge of the blade suction side, where low-pressure zone was established under the effect of centrifugation, and then gradually propagated to downstream passages in a centrifugal pump by numerical calculations. Li *et al.* [2021] experimentally studied the influence of temperature on the cavitation behaviors of an engine cooling water pump. The results show that cavitation happens more easily at higher temperature, which corresponds to the higher vaporization pressure.

In centrifugal pumps, the interaction between the rotating impeller and the static volute will cause pressure pulsation. Furthermore, the generation and collapse of vapor bubbles caused by cavitation also leads to unsteady pressure pulsation and force fluctuation. For example, Li *et al.* [2017] conducted numerical studies on the unsteady cavitation flow in a high-speed micro centrifugal pump and concluded that the amplitudes of pressure fluctuations on the blade pressure surface were bigger at cavitation conditions, but on the suction surface, the situation was on the contrary. Dong *et al.* [2019] numerically investigated the variation of radial force of centrifugal pumps under different cavitation stages. The results demonstrate that with the development of cavitation, the radial force on the impeller tends to remain invariable first and then decrease, and the trail of the radial force changes from closed to open. It can be observed that cavitation can give rise to pressure pulsation, radial force fluctuation, consequent noise and vibration [Gangipamula *et al.*, 2022; Lu *et al.*, 2022; Zhang *et al.*, 2015, 2018]. Particularly for the levitated micropump, radial force fluctuation caused by cavitation may lead to the deviation of the rotor from equilibrium position, thus, changing the structure of the levitated micropump. And the change of structure can influence the anti-cavitation performance of pumps, which has attracted extensive attention from researchers. Luo *et al.* [2008] analyzed the internal flow field of a miniature pump by numerical simulation, suggesting that the anti-cavitation performance of miniature pumps would decline as the axial

tip clearance increased. Hao and Tan [2018] investigated the cavitating flows of a mixed-flow pump as turbine (PAT) at pump mode, and revealed that in comparison with the symmetrical tip clearance, the asymmetrical tip clearance made the PAT cavitation performance worse.

In the levitated micropump, the impeller rotates eccentrically in the volute and the change of eccentricity will result in the change of the structure, thus, influencing the anti-cavitation performance. The development of cavitation will cause radial force fluctuation, which can change the eccentricity further. Therefore, to explore the complex coupling relationship between cavitation and eccentric rotation, further investigation on the cavitation flow in the levitated micropump is urgently needed.

In this paper, the development of cavitation flow in the levitated micropump has been investigated based on numerical simulation and experiments have been conducted to explore the cavitation external characteristics. The results of simulation agreed well with the experiments. By steady calculations, we analyzed the effects of different eccentricities on the anti-cavitation performance. Then the coupling effects between radial force on the impeller and cavitation were also studied. Finally, unsteady calculations were carried out to capture the pressure pulsation under different cavitation stages. The research results provide an instruction for optimizing the anti-cavitation performance and operating stability of the levitated micropump.

2. Mathematical Methods

2.1. *Geometrical model and parameters*

As shown in Fig. 1(a), the levitated micropump is comprised of a volute, an open impeller and a motor. The motor is comprised of the journal bearing, the thrust bearing, the rotor and the stator. Fluid flows into the volute from the inlet and gets energy from the rotating impeller, which enables the fluid to obtain high pressure and high velocity. Finally, the fluid flows away from the outlet. In order to make

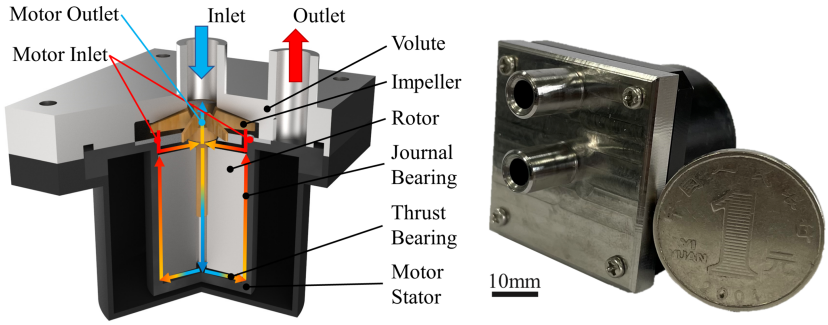

(a) (b)

Fig. 1. (a) Structural schematic diagram and (b) Photograph of the levitated micropump.

the hydrodynamic bearings work, a portion of the fluid is introduced into the motor to fill the gap between the rotor and the stator through the motor inlets and flows back to the volute through the central motor outlet.

Figure 1(b) shows the photograph of the levitated micropump. The size of the levitated micropump is only 34 mm × 34 mm × 42.8 mm, which is small enough even compared to a coin, and the main design parameters of the levitated micropump are shown in Table 1.

2.2. *Computational domain and mesh*

Figure 2(a) presents the computational model used in this study, which only consists of the volute and the impeller for simplifying the problem. Note that compared with the complete structure in Fig. 1(a), the computational model neglects the leak loss from the volute to the motor. Accordingly, numerical results should be modified by volumetric efficiency. To avoid the effect of backflow, the inlet section and the outlet section are extended.

Table 1. Main parameters of the levitated micropump.

Parameters	Value	Parameters	Value
Rotational speed n_d (r/min)	20,000	Impeller inlet diameter D_1 (mm)	4
Flow rate Q_d (m^3/h)	0.156	Impeller outlet diameter D_2 (mm)	14
Head H_d (m)	10	Blade outlet width b_2 (mm)	1
Specific speed n_s	85.5	Blade outlet angle β_2 (deg)	90
Number of blades Z	8	Inlet diameter of pump D_3 (mm)	4.2
Volute inlet diameter D_0 (mm)	15	Outlet diameter of pump D_4 (mm)	4.2

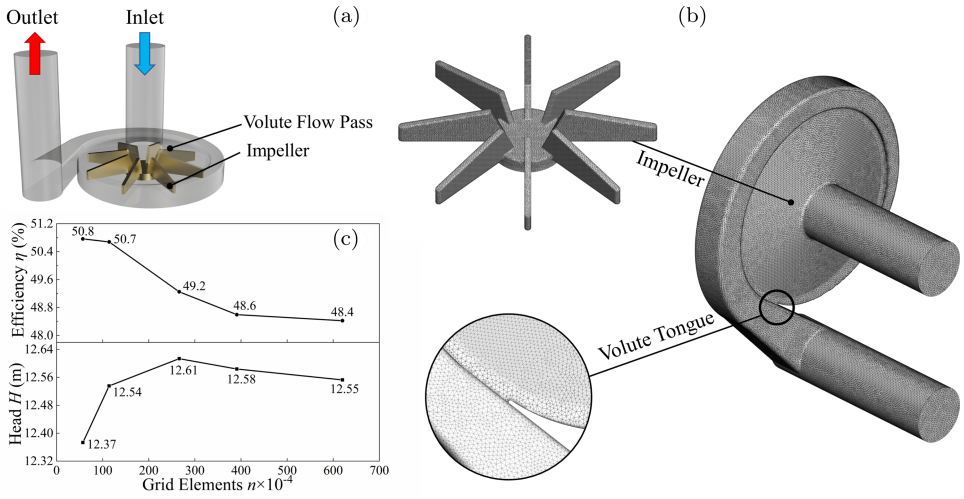

Fig. 2. (a) Computational model. (b) Grids of the impeller and volute. (c) Grid independence analysis.

Unstructured tetrahedral meshes were used in the entire flow domains, because of their good adaptability for complicated geometries. And finer meshes were adopted near the blade surfaces and the volute tongue to capture flow details and improve the calculation accuracy. Figure 2(b) shows the grids and the details of the impeller and the volute tongue, and the value of $y+$ is less than 60 on the impeller surfaces.

Five sets of different grids were used for grid independence study of steady calculation at noncavitation conditions. The results of grid independence analysis are presented in Fig. 2(c), and it can be seen that the fluctuations of the head and hydraulic efficiency are both less than 0.4% when grid elements are greater than 3.91×10^6. Therefore, the mesh with 3.91×10^6 elements is adopted, and when the structural parameters of the levitated micropump change, the meshing strategy and refinement conditions are the same.

2.3. *Governing equations*

In this study, the cavitation flow is regarded as a homogeneous multiphase flow. Due to the high flow velocity of the fluid in the levitated micropump, the slip velocity between the liquid phase and the vapor phase can be neglected. In addition, owing to the ultra-high rotating speed of the levitated micropump, the gravity is relatively small and can also be ignored. The governing equations of the multiphase flow, namely, the mass conservation equations for each phase and the momentum conservation equation for the mixture, can be written as the following forms:

$$\frac{\partial(r_\alpha \rho_\alpha)}{\partial t} + \frac{\partial(r_\alpha \rho_\alpha u_i)}{\partial x_i} = \dot{m}_\alpha, \tag{2.1}$$

$$\frac{\partial(\rho_m u_i)}{\partial t} + \frac{\partial(\rho_m u_j u_i)}{\partial x_j} = -\frac{\partial P}{\partial x_i} + \frac{\partial}{\partial x_j}\left(\mu_m\left(\frac{\partial u_i}{\partial x_j} + \frac{\partial u_j}{\partial x_i}\right)\right), \tag{2.2}$$

where r_α, u_i, ρ_α, $\dot{m}_\alpha$, respectively, represent the volume fraction, Cartesian velocity components, density, and mass generation rate of phase α. α can be replaced by l and v, representing the liquid and the vapor, respectively. t, x_i, and P are time, spatial coordinates and pressure, respectively. ρ_m and μ_m are the volume-weighted mixture density and viscosity, which can be written as follows:

$$\rho_m = r_v \rho_v + (1 - r_v)\rho_l, \tag{2.3}$$

$$\mu_m = r_v \mu_v + (1 - r_v)\mu_l. \tag{2.4}$$

The mass sources have been assumed to arise from interphase mass transfer, and the phases must fill up all the domains. Accordingly, they satisfy the constraints:

$$\dot{m}_l + \dot{m}_v = 0, \tag{2.5}$$

$$r_l + r_v = 1. \tag{2.6}$$

2.4. *Cavitation model*

In this paper, the Zwart–Gerber–Belamri (ZGB) cavitation model is adopted [Zwart *et al.*, 2004], which is deduced from the Rayleigh–Plesset equation and has been widely used to capture the characteristics of the cavitation. The Rayleigh–Plesset equation describes the growth of a vapor bubble in the liquid

$$R_B \frac{d^2 R_B}{dt^2} + \frac{3}{2}\left(\frac{dR_B}{dt}\right)^2 + \frac{2\Theta}{R_B} = \frac{P_v - P}{\rho_l}, \tag{2.7}$$

where R_B is the bubble radius, Θ is the surface tension coefficient, and P_v is the vapor pressure. By neglecting the second-order terms and the surface tension, the expression can be simplified as

$$\frac{dR_B}{dt} = \sqrt{\frac{2}{3}\frac{P_v - P}{\rho_l}}. \tag{2.8}$$

Supposing the mass of a single bubble is m_B, the mass change rate of a single bubble can be calculated by

$$\frac{dm_B}{dt} = \rho_v \frac{d}{dt}\left(\frac{4}{3}\pi R_B^3\right) = 4\pi R_B^2 \rho_v \sqrt{\frac{2}{3}\frac{P_v - P}{\rho_l}}. \tag{2.9}$$

If there are N_B bubbles per unit volume, the vapor volume fraction can be expressed as

$$r_v = \frac{4}{3}\pi R_B^3 N_B. \tag{2.10}$$

Thus, the ZGB model is expressed as follows:

$$\dot{m}_v = F_{\text{vap}} \frac{3 r_{\text{nuc}}(1 - r_v)\rho_v}{R_B} \sqrt{\frac{2}{3}\frac{P_v - P}{\rho_l}}, \quad \text{if } P < P_v, \tag{2.11}$$

$$\dot{m}_l = F_{\text{cond}} \frac{3 r_v \rho_v}{R_B} \sqrt{\frac{2}{3}\frac{P - P_v}{\rho_l}}, \quad \text{if } P > P_v, \tag{2.12}$$

where F_{cond} and F_{vap} are empirical constants, r_{nuc} is the nucleation site volume fraction. The model parameters are $R_B = 10^{-6}$ m, $r_{\text{nuc}} = 5 \times 10^{-4}$, $F_{\text{vap}} = 50$, and $F_{\text{cond}} = 0.01$.

The vapor pressure P_v is usually chosen as a constant according to the test temperature, whereas P_v is also affected by the local turbulence pressure fluctuation. Therefore, taking the effect of the local turbulent pressure fluctuation into consideration, P_v can be modified as

$$P_v = P_{\text{sat}} + 0.195 \rho_m k, \tag{2.13}$$

where P_{sat} is the saturation pressure at the test temperature, and k is the turbulent kinetic energy [Singhal *et al.*, 2002].

Table 2. Fluid properties.

P_{sat} (Pa)	ρ_l (kg/m3)	ρ_v (kg/m3)	μ_l (Pa·s)	μ_v (Pa·s)
31,200	977.78	0.1978	4.039×10^{-4}	1.126×10^{-5}

2.5. *Computation scheme*

The numerical calculation in this study was conducted based on ANSYS FLUENT. The total pressure inlet is specified for the inlet boundary, and the outlet boundary is set up as mass flow outlet. No-slip conditions are applied on the solid walls. The fluid domain of the impeller is set as a moving coordinate system with the rotating speed of 20,000 r/min, while the static coordinate system is adopted for the volute domain. The interfaces are established between the rotational domain and the stationary domain to transfer data. Considering the heat fluxes from other components in the microfluidic system, the working fluid is set as water with 70°C, and the corresponding fluid properties are listed in Table 2.

The realizable $k-\epsilon$ turbulence model is selected to account for the transport of the turbulent shear stress, which can obtain an effective solution for the flow field with strong rotation and large flow curvature [Shih *et al.*, 1995]. Unsteady cavitation calculations are performed based on the results of steady calculations, and the time step is set to $\Delta t = 8.3333 \times 10^{-6}$ s, equivalent to the time interval for the impeller to rotate 1°. After the first six rotation cycles, the calculation results have shown periodical unsteady fluctuation, indicating that the calculation is convergent.

3. Results and Discussion

3.1. *Cavitation characteristics*

First, a performance test is conducted in order to obtain the cavitation characteristic curves of the levitated micropump and verify the accuracy of the numerical results. Figure 3(a) shows the test bench system. The water temperature could be adjusted by the water bath kettle (HH-1-3L type) with a deviation of ± 0.5°C. The inlet total pressure of the levitated micropump is controlled by the inlet valve. Simultaneously, flow rate is kept constant by the outlet valve and measured by the turbine flowmeter (YF-S401 type) with an error of ±2%. Both the inlet pressure and the outlet pressure are obtained by the pressure transmitters (SUP-Y810 type) with the full scale accuracy of 0.5%. The ranges of the pressure transmitters are −0.1–0.1 MPa at the inlet and 0–250 kPa at the outlet of the levitated micropump.

As mentioned above, compared with the complete structure of the levitated micropump, the computational model neglects the leak loss from the volute to the motor. Therefore, the head needs to be corrected by the volumetric efficiency η_v.

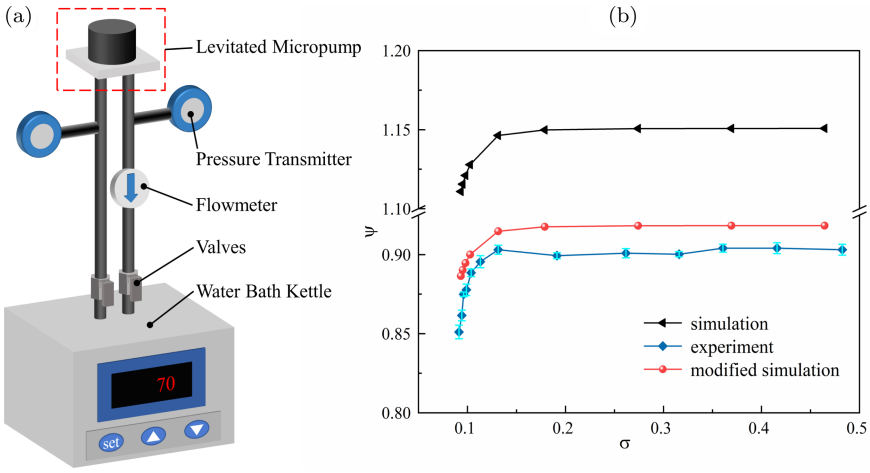

Fig. 3. (a) Test bench system. (b) Head coefficient with cavitation number.

η_v can be calculated by

$$\eta_v = \frac{\rho_l g Q H}{\rho_l g Q H + \rho_l g q (P_{mi} - P_{mo})}, \tag{3.1}$$

where g is the acceleration of gravity, Q and H represent the flow rate and the head of the levitated micropump, respectively, q is the leakage rate from the volute to the motor, P_{mi} and P_{mo} represent the pressure of the motor inlet and the motor outlet, respectively. By calculating the simulation model of the whole micropump, we obtained the value of η_v, which is equal to 79.8%.

The inlet pressure and the pressure head of the levitated micropump can be transformed into dimensionless forms by the following formulas:

$$\sigma = \frac{P_{\text{tin}} - P_{\text{sat}}}{0.5 \rho_l u_2^2}, \tag{3.2}$$

$$\psi = \frac{2gH}{u_2^2}, \tag{3.3}$$

where P_{tin} is the inlet total pressure, and u_2 is the tangential velocity at the blade outlet. Figure 3(b) shows the comparison between the experimental results and the numerical results of the cavitation characteristic curves at Q_d. It can be observed that the head coefficient ψ generally shows a downward trend with the decrease of the cavitation number σ. Under high cavitation number, the head coefficient almost remains constant but has a sharp decline when the cavitation number is decreased to a critical value. The trend of the head coefficient obtained by numerical simulation is highly consistent with experimental results. Furthermore, the numerically predicted head coefficient modified by the volumetric efficiency has a high degree of accuracy compared with the experimental results. The max error is within 2%

under noncavitation stage. Note that the modified head coefficient is still higher than the experimental results, which can be attributed to the flow resistance in actual pipelines and the wall roughness, etc.

The critical cavitation number σ_c is a valuable cavitation number to evaluate the anti-cavitation performance, which corresponds to the 3% drop in head coefficient [Cao *et al.*, 2022; Li *et al.*, 2017; Lu *et al.*, 2016]. As seen in Fig. 3(b), the critical cavitation numbers σ_c for the experimental results and numerical results are about 0.0973 and 0.0955, respectively. The error between the experiment and the simulation is only 1.8%. These results show that the numerical methods in this study have good accuracy.

3.2. *Analysis of the development process of cavitation*

Figure 4(a) shows the development of cavitation in the impeller under different cavitation numbers at Q_d, which is described by isosurfaces of the 10% vapor volume fraction. It could be found that vapor bubbles do not exist in the impeller at the beginning. With the cavitation number falling to 0.1313, vapor bubbles are observed to occur near the leading edge of the suction side of the blades. When the cavitation number is further decreased to 0.0952, vapor bubbles gradually extend to the blade outlet and occupy almost half of the flow passages between the blades, causing the blockage of flow which leads to the sharp drop of the head coefficient, as shown in Fig. 3(b).

Figure 4(b) presents the static pressure distribution at the midspan of the impeller at Q_d. The low-pressure area initially appears near the leading edge of

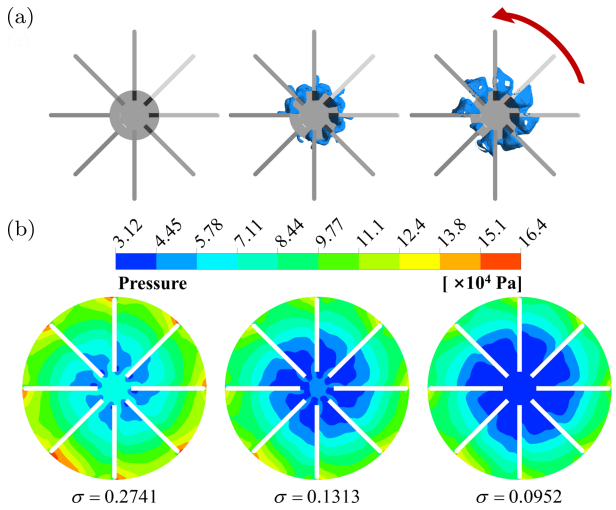

Fig. 4. (a) Vapor bubbles distribution in the impeller and (b) Static pressure distribution at the midspan of the impeller at Q_d under different cavitation numbers.

the suction side of the blades. With the decrease of cavitation number, the low-pressure area expands to the outlet of the blades, corresponding to the results of Fig. 4(a). Moreover, the distribution of pressure at the midspan of the impeller is asymmetric due to the interaction between the rotating impeller and the static volute, leading to the asymmetric distribution of vapor bubbles. The blade facing the outlet of the pressurized water chamber has the least vapor bubbles, which may be attributed to the high pressure at the outlet of the pressurized water chamber.

3.3. *Effects of eccentricity on the anti-cavitation performance*

The radial suspension force is provided by the journal bearing designed according to hydrodynamic lubrication theory [Pinkus and Sternlicht, 1961]. Figure 5(a) shows the structure of the journal bearing, which is comprised of a rotating journal (rotor) and a sleeve with a small clearance between them filled with fluid. The rotor rotates eccentrically and forms a wedge clearance with the sleeve. Positive pressure is generated in zone I and negative pressure is generated in zone II. This phenomenon provides the bearing capacity to balance the external force and make

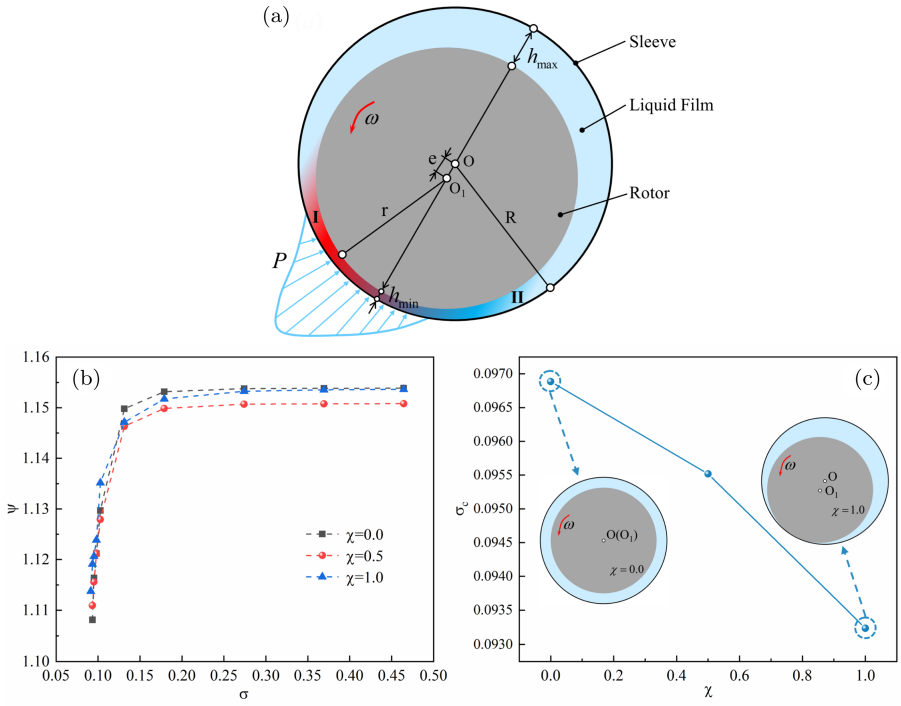

Fig. 5. (a) Schematic diagram of the journal bearing. (b) Head coefficient with cavitation number under different eccentricities. (c) Critical cavitation number with eccentricity.

the rotor suspended. In order to further explore the influence of the eccentricity on the anti-cavitation performance, the results when eccentricity χ is 0, 0.5, and 1 are calculated. The eccentricity χ is defined as

$$\chi = \frac{e}{R - r}, \tag{3.4}$$

where e is the eccentric distance, R and r, respectively, represent the radius of the sleeve and the rotor.

Figure 5(b) shows the cavitation characteristic curves under different eccentricities. It can be observed that the head coefficient under noncavitation stage almost remains the same under different eccentricities, as well as the trend of head coefficient with cavitation number. Figure 5(c) presents the trend of critical cavitation number with eccentricity. The critical cavitation number is almost linear with the eccentricity. With the increase of the eccentricity, the critical cavitation number of the levitated micropump decreases gradually, implying the anti-cavitation ability gradually increases.

Figure 6(a) shows the vapor volume fraction at the midspan of the impeller under different eccentricities. The vapor volume fraction near the blades (b1–b3) has a decline with the increase of the eccentricity, while has a rise near the blade (b4). For other blades, there is no significant change in vapor volume fraction. To observe the change of vapor volume fraction more clearly, flow variables are displayed on a cylinder with a radius of 2.5 mm from the center of the impeller. Figure 6(b) shows the vapor volume fraction on the cylinder. The vapor volume fraction near the blade (b1) has an obvious reduction with the increase of the eccentricity, which can be explained as the shrink of low-pressure area, as illustrated in Fig. 6(c). Moreover, Table 3 compares the vapor volume fraction in rotational domain under different eccentricities. It can be observed that the vapor volume fraction in rotational domain decreases gradually with the increase of eccentricity, and has a reduction of 14.8% from $\chi = 0$ to $\chi = 1.0$.

Figure 6(d) depicts the velocity fields on vertical section across the centerline of the impeller under different eccentricities. It can be observed that the velocity of the fluid above the left blade increases with the eccentricity, while the velocity of the fluid above the right blade decreases with the eccentricity. Note that due to the eccentric movement of the impeller, the left blade is exactly the blade on the side close to the inlet of the volute, while the right blade is further. Consequently, it can be concluded that the position of the blades leads to the contrary variation trend of velocity with eccentricity. For the right blades, the velocity near the leading edge becomes lower and the pressure has a rise, thus, enhancing the anti-cavitation ability. But the situation is reversed on the left blades. It can be implied that the enhanced anti-cavitation effect overall outweighs the weakened anti-cavitation effect, and thus, the eccentric rotation finally improves the anti-cavitation ability of the levitated micropump.

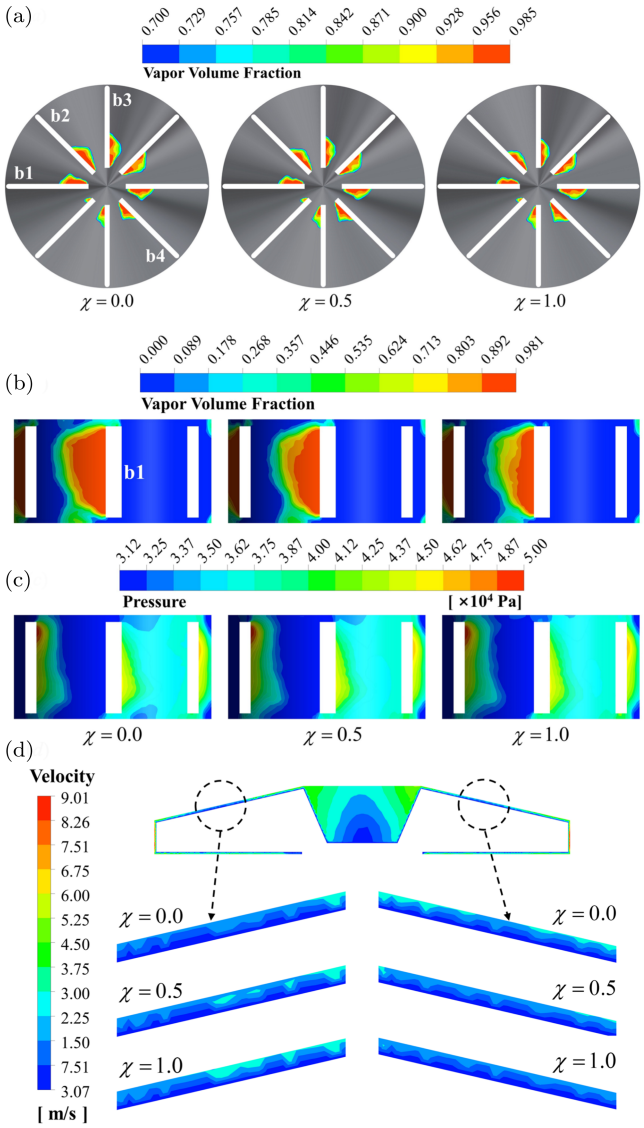

Fig. 6. (a) Vapor volume fraction at the midspan of the impeller under different eccentricities. Flow variables on the cylindrical slice with a radius of 2.5 mm from the center of the impeller under different eccentricities: (b) Vapor volume fraction and (c) Static pressure. (d) Velocity on the vertical section across the centerline of the impeller under different eccentricities.

3.4. *Coupling effects between radial force on the impeller and cavitation*

The impeller is subjected to radial force exerted by the fluid, which results in the eccentric rotation. However, as the cavitation develops, the magnitude of radial

Table 3. Vapor volume fraction in rotational domain under different eccentricities.

χ	0.0	0.5	1.0
Vapor volume fraction (%)	6.22	5.70	5.30

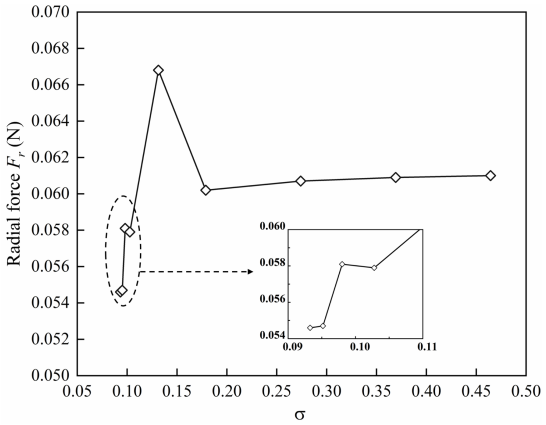

Fig. 7. Radial force on the impeller with cavitation number.

force will change. Figure 7 shows the radial force on the impeller with the cavitation number under $\chi = 0.5$. With the decrease of cavitation number, the radial force gradually declines at first, then has a sudden increase and finally reduces with fluctuation. The sudden rise in radial force, which can be attributed to the inception of cavitation, will lead to an increase in eccentricity. As a result, the rotor may contact the sleeve and suspension failure may happen. As the cavitation develops further, the radial force turns to decrease, causing a decline in eccentricity. While the decrease of eccentricity will further result in the deterioration of cavitation according to Fig. 5(c). This unique phenomenon in the levitated micropump owes to the coupling effects between cavitation and radial force.

3.5. *Effects of cavitation on pressure pulsation*

The interaction between the rotating impeller and the static volute leads to pressure pulsation in pumps. Additionally, the generation and collapse of vapor bubbles caused by cavitation also have an impact on pressure pulsation. To investigate the effects of cavitation on pressure pulsation, unsteady numerical simulations are carried out and 5 monitoring points are set up as shown in Fig. 8(a). To analyze the frequency characteristics of pressure pulsation, the fast Fourier transform (FFT) is used for the static pressure coefficient, as shown in Fig. 8(b). The static pressure coefficient is defined as

$$C_p = \frac{P_s - P_a}{0.5\rho_l u_2^2}, \tag{3.5}$$

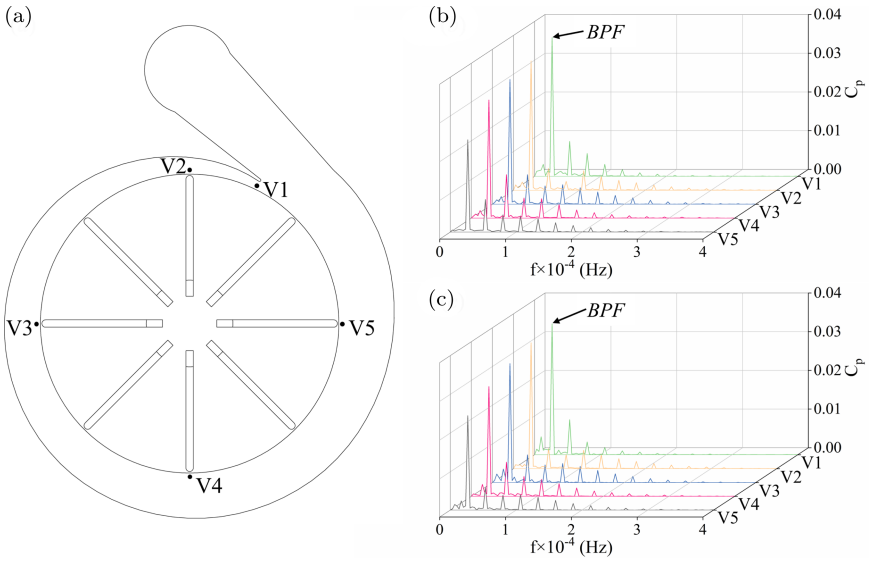

Fig. 8. (a) Monitoring points. FFT results of static pressure coefficient at monitoring points: (b) Noncavitation and (c) Critical cavitation.

where P_s and P_a are the static pressure at the monitoring point and the average static pressure at the monitoring point during one rotation period, respectively. The results show that the predominant frequencies of pressure pulsation are the blade passing frequency (BPF) and the harmonic frequency of BPF under both noncavitation and critical cavitation. The amplitude of pressure pulsation at $V1$ is the highest, which can be explained by the strongest interaction between the impeller and the volute at the volute tongue. Moreover, the amplitude of BPF has a drop under critical cavitation, which may be attributed to the decrease of head coefficient caused by cavitation, except for $V5$. However, the amplitude of low frequency less than BPF becomes larger under critical cavitation except for $V2$, indicating that the generation and collapse of vapor bubbles can cause low-frequency pressure pulsation.

4. Conclusions

To reveal the cavitation flow characteristics in the hydrodynamic levitated micropump, numerical and experimental investigations were carried out in this paper. Considering the unique eccentric rotation of the levitated micropump, the effects of eccentricity on the anti-cavitation performance were analyzed by numerical simulation. The coupling effects between the radial force on the impeller and cavitation were also explored. In addition, the unsteady pressure pulsation in the volute was analyzed with the development of cavitation. The main conclusions are summarized

as follows:

(1) The accuracy of numerical simulation was verified via comparison with the experimental results. The trend of the head coefficient obtained by numerical simulation is highly consistent with the experimental results. The critical cavitation numbers σ_c for the experimental results and numerical results are about 0.0973 and 0.0955, respectively, between which the error is only 1.8%.
(2) With the decrease of cavitation number, vapor bubbles are observed to occur near the leading edge of the suction side of the blades and gradually extend to the blade outlet, causing the blockage of flow. The distribution of pressure at the midspan of the impeller is asymmetric due to the interaction between the rotating impeller and the static volute, thus, leading to the asymmetric distribution of vapor bubbles.
(3) The critical cavitation number is approximately linear with the eccentricity. As the eccentricity increases, the critical cavitation number gradually decreases, indicating that the eccentric rotation is beneficial to improve the anti-cavitation ability of the levitated micropump. For the blades on the side away from the inlet of the volute, the velocity near the leading edge becomes lower and the pressure has a rise. While for the blades on the side close to the inlet of the volute, the situation is reversed.
(4) With the decrease of cavitation number, the radial force on the impeller gradually declines at first, then has a sudden increase and finally reduces down with fluctuation. The sudden rise in radial force may result in the contact between the rotor and the sleeve, and may give rise to suspension failure. As the cavitation develops further, the radial force turns to decrease, causing a decline in eccentricity, which will further result in the deterioration of cavitation.
(5) The predominant frequencies of pressure pulsation are the BPF and the harmonic frequency of BPF under both noncavitation and critical cavitation. Owing to the strongest interaction between the impeller and the volute at the volute tongue, the amplitude of pressure pulsation at $V1$ is the highest. Under critical cavitation, the amplitude of BPF has a drop except for $V5$. However, the amplitude of low frequency less than BPF becomes larger except for $V2$.

Acknowledgments

This work was supported by Open Fund of Science and Technology on Thermal Energy and Power Laboratory (No. TPL2018B03).

References

Cao, W. D., Jia, Z. X., Zhao, Z. J. and Zhou, L. [2022] "Validation and simulation of cavitation flow in a centrifugal pump by filter-based turbulence model," *Engineering Applications of Computational Fluid Mechanics* **16**(1), 1724–1738.

Dong, L., Shang, H. H., Zhao, Y. Q., Liu, H. L., Dai, C. and Wang, Y. [2019] "Study on unstable characteristics of centrifugal pump under different cavitation stages," *Journal of Thermal Science* **28**(4), 608–620.

Gangipamula, R., Ranjan, P. and Patil, R. S. [2022] "Flow-induced noise sources and reduction methods in centrifugal pumps: A literature review," *Physics of Fluids* **34**(8), 081302.

Hao, Y. and Tan, L. [2018] "Symmetrical and unsymmetrical tip clearances on cavitation performance and radial force of a mixed flow pump as turbine at pump mode," *Renewable Energy* **127**, 368–376.

Hatami, H., Bagheri, A. and Ansari, R. [2020] "An analytical investigation for vibration characteristics of a beam-type liquid micro-pump," *International Journal of Applied Mechanics* **12**(2), 2050016.

Laser, D. J. and Santiago, J. G. [2004] "A review of micropumps," *Journal of Micromechanics and Microengineering* **14**(6), R35–R64.

Li, Y. Q., Yuan, S. W. and Lai, H. X. [2017] "Numerical study of unsteady flows with cavitation in a high-speed micro centrifugal pump," *Journal of Thermal Science* **26**(1), 18–24.

Li, W., Wu, P., Yang, Y. F., Shi, W. D. and Li, W. Q. [2021] "Investigation of the cavitation performance in an engine cooling water pump at different temperature," *Proceedings of the Institution of Mechanical Engineers, Part A: Journal of Power and Energy* **235**(5), 1094–1102.

Lu, J. X., Yuan, S. Q., Luo, Y., Yuan, J. P., Zhou, B. L. and Sun, H. [2016] "Numerical and experimental investigation on the development of cavitation in a centrifugal pump," *Proceedings of the Institution of Mechanical Engineers, Part E: Journal of Process Mechanical Engineering* **230**(3), 171–182.

Lu, Y. P., Tan, L., Han, Y. D. and Liu, M. [2022] "Cavitation-vibration correlation of a mixed flow pump under steady state and fast start-up conditions by experiment," *Ocean Engineering* **251**, 111158.

Luo, X. W., Liu, S. H., Zhang, Y. and Xu, H. Y. [2008] "Cavitation in semi-open centrifugal impellers for a miniature pump," *Frontiers in Energy* **2**(1), 31–35.

Luo, X. W., Ji, B. and Tsujimoto, Y. [2016a] "A review of cavitation in hydraulic machinery," *Journal of Hydrodynamics* **28**(3), 335–358.

Luo, X. B., Liu, F. L., Duan, B., Wu, H., Hu, J. Y. and Yu, X. J. [2016b] "A hydrodynamic levitated mechanical micropump," US Patent, US 10495093.

Luo, X. B., Liu, F. L., Duan, B., Wu, H., Wu, R. K., Yu, X. J. and Hu, J. Y. [2017a] "A fluid hydrodynamic suspension mechanical pump," Chinese Patent, ZL 201710228549.X.

Luo, X. B., Wu, R. K., Duan, B. and Liu, F. L. [2017b] "A hydrodynamic levitated mechanical pump with grooved bearings," Chinese Patent, ZL 201710339001.2.

Luo, X. B., Duan, B., Liu, F. L. and Wu, R. K. [2017c] "A self-circulation liquid cooling micropump," Chinese Patent, ZL 201710339480.8.

Mohith, S., Karanth, P. N. and Kulkarni, S. M. [2019] "Recent trends in mechanical micropumps and their applications: A review," *Mechatronics* **60**, 34–55.

Nguyen, N. T., Huang, X. Y. and Chuan, T. K. [2002] "Mems-micropumps: A review," *Journal of Fluids Engineering-Transactions of the ASME* **124**(2), 384–392.

Pinkus, O. and Sternlicht, B. [1961] *Theory of Hydrodynamic Lubrication* (McGraw-Hill, Inc., New York).

Shih, T. H., Liou, W. W., Shabbir, A., Yang, Z. G. and Zhu, J. [1995] "A new k–ϵ Eddy viscosity model for high Reynolds number turbulent flows," *Computers & Fluids* **24**(3), 227–238.

Singhal, A. K., Athavale, M. M., Li, H. Y. and Jiang, Y. [2002] "Mathematical basis and validation of the full cavitation model," *Journal of Fluids Engineering-Transactions of the ASME* **124**(3), 617–624.

Woias, P. [2005] "Micropumps — Past, progress and future prospects," *Sensors and Actuators B*: *Chemical* **105**(1), 28–38.

Zhang, N., Yang, M. G., Gao, B. and Li, Z. [2015] "Vibration characteristics induced by cavitation in a centrifugal pump with slope volute," *Shock and Vibration* **2015**, 1–10.

Zhang, N., Gao, B., Li, Z. and Jiang, Q. F. [2018] "Cavitating flow-induced unsteady pressure pulsations in a low specific speed centrifugal pump," *Royal Society Open Science* **5**(7), 180408.

Zwart, P., Gerber, A. G. and Belamri, T. [2004] "A two-phase flow model for predicting cavitation dynamics," *5th International Conference on Multiphase Flow*, Vol. 152, Yokohama, Japan, Paper No. 152.